ISSN 1027-4510, Journal of Surface Investigation. X-ray, Synchrotron and Neutron Techniques, 2007, Vol. 1, No. 5, pp. 542–555. © Pleiades Publishing, Ltd., 2007.
Original Russian Text © A.I. Okorokov, S.V. Grigor'ev, V.V. Runov, G.P. Gordeev, Yu.O. Chetverikov, G.P. Kopitsa, 2007, published in Poverkhnost'. Rentgenovskie, Sinkhrotronnye i Neitronnye Issledovaniya, No. 9, pp. 49–62.

New Magnetic Phenomena and Polarized Neutrons

A. I. Okorokov, S. V. Grigor'ev, V. V. Runov, G. P. Gordeev, Yu. O. Chetverikov, and G. P. Kopitsa

St. Petersburg Nuclear Physics Institute, Russian Academy of Sciences, Gatchina, Leningrad oblast, 188300 Russia

Received April 4, 2007

Abstract—The results of recent investigations into new magnetic phenomena by means of small-angle polarized neutron scattering are reviewed. In particular, the problem of spin chirality observed in a helical structure of MnSi, which has provided a deeper insight into the properties of cubic magnets without the center of inversion, is analyzed. More recently, spin chirality has been observed in a Dy/Y multilayer structure. Using polarized neutron scattering, the temperature dependence of the spin wave stiffness D_0 in a Fe–Ni alloy (Invar) has been studied and for the first time it is established that it is well fitted by the power law $D = D_0\tau^x$ with $x \cong 0.5$ in the entire ferromagnetic range of temperatures: $\tau = 1 - T/T_C$ from 0.1 to 0.9. The results of the first neutron investigations of the mesostructure of alloys possessing magnetic shape memory are considered. Data on the structural ordering of Fe_3O_4 magnetic nanoparticles in a D_2O-based ferrofluid on a single crystal silicon surface are considered. The original observations of neutron scattering on heavy-fermion quasi-particles are described and discussed.

DOI: 10.1134/S1027451007050072

1. INTRODUCTION

Experiments with spin-polarized neutrons (in contrast to those with unpolarized particles) involve, in addition to wave vector transfer **q** and energy transfer ω, polarization parameter **P**. In magnetic scattering measurements, this factor provides additional information that in most cases cannot be obtained by other methods. The unique possibilities offered by polarized (in contrast to unpolarized) neutrons are related to the fact that the magnetic scattering cross section depends on the mutual orientation of the sample magnetization $\mathbf{m} = \mathbf{M}/M$, scattering vector $\mathbf{e} = \mathbf{q}/q$, and initial neutron velocity **v** (or wave vector $\mathbf{k}_0$). As long ago as 1939, Halpern and

Johnson [1] established a relation $\mathbf{P} = -\mathbf{e}(\mathbf{e}\mathbf{P}_0)$ between the polarization **P** and the scattering vector **e**, and found a pseudovector $\mathbf{M}_\perp = \mathbf{m} - (\mathbf{em})\mathbf{e}$ in the scattering cross section that described the magnetic-nuclear interference. Later, Maleyev [2] found $\mathbf{M}_\parallel = (\mathbf{em})\mathbf{e}$ pseudovector for purely magnetic scattering and $\mathbf{n} = [\mathbf{k}', \mathbf{k}_0]/|[\mathbf{k}', \mathbf{k}_0]|$ pseudovector [3] for a higher, above Born, approximation along which the polarization can be oriented upon scattering on three-spin correlations.

All the aforementioned pseudovectors have been used in our experimental investigations of various magnetic interactions by means of small-angle polarized neutron scattering.

2. EXPERIMENTAL METHODS

The relation $\mathbf{P} = -\mathbf{e}(\mathbf{e}\mathbf{P}_0)$ plays a determining role in the polarization analysis of small-angle neutron scattering. Indeed, once vector **P** is determined, we know the direction of the scattering vector **q** and then calculate the magnitude of this vector using the scheme of scattering, since the initial wave vector $\mathbf{k}_0$ and the scattering angle θ are set by the experimental setup. Thus, the measurement of polarization **P** provides complete information about the scattering: the knowledge of polarization components P_x, P_y, and P_z makes it possible to separately determine the elastic (for P_x and P_y perpendicular to the beam axis) and inelastic (for P_z parallel to the beam axis) magnetic scattering, while the sum rule $P_x/P_{0x} + P_y/P_{0y} + P_z/P_{0z} = -1$ allows the nuclear scattering and the detector background to be evaluated.

In order to realize these possibilities, a three-dimensional (3D) analyzer of the polarization of scattered neutrons was created [4], which allowed the polarization of the primary neutron beam to be sequentially set parallel to the *X*, *Y*, and *Z* coordinate axes, and the corresponding polarization components P P_x, P_y, and P_z, respectively, to be measured.

Using the phenomenon of neutron depolarization on magnetic domains, it is possible to evaluate the domain size and determine the parameters of magnetic texture from the depolarization anisotropy coefficient $A_d = \ln(P_{x,y})/\ln(P_z)$ [5], that is, to study the texture and the magnetostriction effects. If a magnetic field **B** penetrates inside the sample, the vector **P** will exhibit Larmor precession $d\mathbf{P}(t)/dt = \gamma[\mathbf{P}(t), \mathbf{B}]$ and, by measuring the rotation of **P**, it is possible to judge the magnitude and direction of **B** in the sample.

The use of spin-polarized neutrons in small-angle neutron scattering makes it possible to study the spin

dynamics without energy analysis, by measuring only the polarization characteristics. The theoretical works of Maleyev et al. and the results of experiments [6] on the critical spin dynamics in iron performed using the 3D polarization analyzer [4] fully confirmed the unique potential of polarized neutrons. In these experiments, the critical static ($\nu = 0.67 \pm 0.01$) and dynamic ($z = 2.617 \pm 0.04$) indices for the transition of Fe into a ferromagnetic state were determined for the first time with a high accuracy in a range of relative temperatures $\tau = (T - T_C)/T_C$ two orders of magnitude wider than that in other investigations. The measurements were performed in the region of very small energy transfer (with a sensitivity threshold of 10^{-7} eV per 1% polarization change at $\lambda = 1$ nm and $\theta = 10^{-2}$ rad), which was inaccessible to standard neutron spectrometry. Thus, the validity of the scaling hypothesis in critical phenomena was confirmed. The experiments also confirmed the anisotropy of the neutron beam depolarization on magnetically isotropic inhomogeneities—a new physical phenomenon that had been theoretically predicted earlier, revealed a difference between the dynamic form factor and the Lorentz function in the high-frequency limit and demonstrated the important possibility of experimental investigations of the asymptotic properties of the Green function of ferromagnets.

Another important achievement was the theoretical prediction and experimental detection of three-spin (chiral or screw) dynamic correlations $C^{(3)} = \langle S_1^x(t_1) S_2^y(t_2) S_3^z(t_3) \rangle$ [3, 7]. The relative scattering cross section on these correlations is negligibly small (on the order of 10^{-5}), but it was found that the cross section must increase in the critical paramagnetic region near T_C and the scattering must exhibit a left–right asymmetry (LRA) relative to the $\mathbf{n} = [\mathbf{k}', \mathbf{k}_0]/|[\mathbf{k}', \mathbf{k}_0]|$ direction. The corresponding experiment was carried out at the St. Petersburg Nuclear Physics Institute (Gatchina) using an iron sample in a zero magnetic field, and the chiral scattering component was measured for the first time. The asymmetry was at a level of 1.5×10^{-4} and exhibited a temperature dependence of the $1/\tau$ type, in agreement with theory.

In a magnetized sample, the $\mathbf{M}_\parallel = (\mathbf{em})\mathbf{e}$ pseudovector operates and the z-component $S_3^z(t_3)$ is fixed by the magnetic field in the $C^{(3)}$ correlator. Under certain experimental conditions (oblique magnetic field) related to the parity of the antisymmetric part of the inelastic neutron scattering cross section [8], it is possible to observe spin-wave excitations described by the $\langle S_1^x(t_1) S_2^y(t_2) \rangle$ correlator. The spin-wave part of the cross section exhibits LRA and is readily separated in experiment.

The LRA method was used in the first thorough investigation into the spin dynamics in iron in magnetic field [9], where fundamentally new results were obtained: the odd, in terms of energy, spectra of three-spin correlations were observed, a "stiff" critical dipole dynamics in iron was established, and the hypothesis concerning factorization in the momentum dependence of triple dynamic vertices for large momentum transfer was confirmed. In contrast to common spectrometers (where the spin-wave stiffness D is determined from the $\mathbf{q}$-dependence of the energy transfer ω), the D value for the LRA measurements in oblique geometry is determined in a very simple manner: the maximum angle of neutron scattering on a magnon is equal to the ratio of the magnon and neutron masses, $\theta_c = (h/2\pi)^2/2Dm_n$, which yields $D(\text{meV Å}^2) = 2072/\theta_c$ (mrad). This method was used to study amorphous magnets [10], Fe–Ni (Invar) alloys [11], and many other magnetic materials. A complicated relief of a large data array on neutron scattering observed using a two-coordinate (XY) detector (128 × 128 pixels) ensures high accuracy of the extracted parameters. For example, for the amorphous alloy $Fe_{50}Ni_{22}Cr_{10}P_{18}$, we have a stiffness of $D = 52.74 \pm 0.05$ meV Å^2, a dipole constant of $\omega_0\langle S_z \rangle = (50 \pm 3) \times 10^{-6}$ eV, and a damping constant of $\Gamma_0(kR_c) = 25.2 \pm 0.5$. Figure 1 shows the pattern of neutron scattering on this amorphous magnet.

3. CHIRALITY OF MANGANESE SILICIDE CRYSTAL

The chirality (handedness) is a basic characteristic of substances with helical (spiral) structures, which are frequently encountered in nature, including both organic (living) and inorganic matter. Substances such as proteins and DNA play a very important role, and the elucidation of the relationship between their essential properties and chirality is among the urgent problems. The spiral (helical) ordering of magnetic moments (spins) is also frequently encountered in magnets, where the problems of chirality constantly attract the attention of both theorists and experimenters.

In 1985, Kawamura [12] put forward a hypothesis that the transition to a chiral spin structure in magnets belongs to a new class of universality in second-order phase transitions having specific chiral critical indices (exponents). This hypothesis was confirmed for the first time by means of polarized neutron scattering on a triangular-lattice $CsMnBr_3$ antiferromagnet [13]. In helical magnets such as Ho, chirality is difficult to study because the domains with left- and right-handed helices have equal populations (n_l and n_r, respectively). In order to create a nonequilibrium population ($n_l - n_r \neq 0$) of these domains, it is necessary to use special treatments of the samples, for example, to induce elastic twist deformation. However, this is not necessary in noncentrosymmetric crystals of compounds such as manganese silicide (MnSi), where the chirality is determined by the Dzyaloshinskii–Moriya (DM) interaction potential $V \sim \mathbf{D}_{DM}[\mathbf{S}_1 \times \mathbf{S}_2]$ and has a single preferred direction of rotation as determined by the $\mathbf{D}_{DM}$ vector.

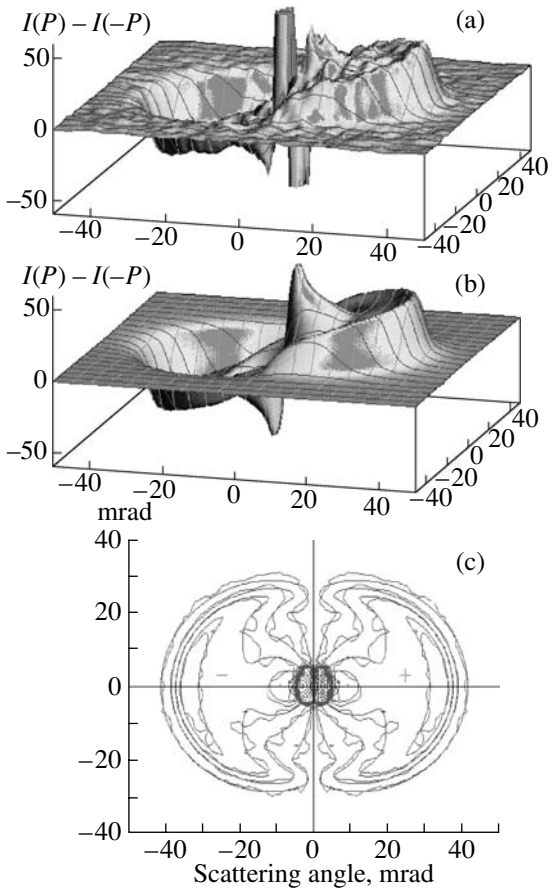

Fig. 1. The typical (a) experimental and (b) theoretical (see text for parameters) patterns of spin-wave scattering $\Delta I = I(P) - I(-P)$ on a $Fe_{50}Ni_{22}Cr_{10}P_{18}$ amorphous alloy; (c) map of the comparison of experimental and theoretical data (smooth curves).

We have studied the properties of MnSi at temperatures both above and below $T_C \approx 29$ K. The dependence of the intensity of small-angle neutrons scattering on their polarization $\mathbf{P}_0$, magnetic field $\mathbf{H}$, and temperature T was measured in a noncentrosymmetric cubic crystal of MnSi, where a left-handed helical spin structure with a superstructural vector $Q = (2\pi/a)(\zeta, \zeta, \zeta)$ ($\zeta = 0.017$) is formed at temperatures below $T_C = 28.7$ K. The unit vector of this helix $\mathbf{m} = [\mathbf{S}_1 \times \mathbf{S}_2]/S^2$ in a demagnetized sample is oriented in the $\langle 111 \rangle$ direction. The elastic neutron scattering cross section $\sigma_{el}(\mathbf{q})$ depends on the mutual orientation of vector $\mathbf{m}$, momentum transfer $\mathbf{q}$, and the initial polarization $\mathbf{P}_0$ [14] as

$$\sigma_{el}(\mathbf{q}) = [rSF(q)/2]^2\{[1 + (\mathbf{qm})^2 + 2(\mathbf{qP}_0)(\mathbf{qm})]\Delta_{\mathbf{q}+Q} + [1 + (\mathbf{qm})^2 - 2(\mathbf{qP}_0)(\mathbf{qm})]\Delta_{\mathbf{q}+Q}\}, \quad (1)$$

where $r = 0.54 \times 10^{-12}$ cm, S is the atomic spin, $\Delta_{\mathbf{q}\pm Q} = [(2\pi)^3/v]\,\delta(\mathbf{q} \pm \mathbf{Q})$, and v is the unit cell volume.

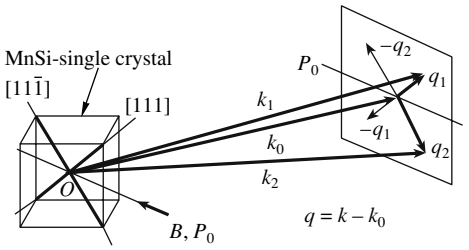

Fig. 2. Experimental geometry for polarized neutron scattering on a MnSi single crystal: **B** is the vector of magnetic induction; $\mathbf{P}_0$ is the initial neutron polarization vector.

The experiments were carried out on the SANS-2 setup of the FRG-1 research reactor in Geesthacht (Germany), using a polarized neutron beam with a wavelength of $\lambda = 5.8$ Å ($\Delta\lambda/\lambda = 0.1$), an initial polarization of $P_0 = 0.96$, and a beam divergence of $\Delta\theta = 2.5$ mrad. Scattered neutrons were detected by a two-coordinate (XY) detector. The measurements were performed in a temperature interval $T = 10$–60 K for a magnetic field $H = 10$–6800 Oe oriented perpendicular to the neutron beam direction. The Bragg scattering intensity on the magnetic helices, $I(q, P_0)$ and $I(q, -P_0)$, was measured and the Bragg reflection polarization $P_p(q, P_0) = \Delta I(q)/I(q)$ was determined, where $\Delta I(q) = I(q, P_0) - I(q, P_0)$ and $I(q) = I(q, P_0) + I(q, P_0)$. The sample crystal was oriented so that two crystallographic axes ([111] and [11$\bar{1}$] and field $\mathbf{H}$ (and, hence, polarization $\mathbf{P}_0$) were in the same plane perpendicular to the incident beam. Figure 2 shows a schematic diagram of the experimental geometry.

3.1. Chirality of MnSi: First Stage of Investigation

(i) The chiral critical fluctuations were observed for the first time at temperatures near and above T_C [15]. The pattern of scattering had the shape of a crescent facing in the direction of the neutron beam polarization (Fig. 3). The radius q of this semicircle in the momentum space is equal to the vector $\mathbf{Q}$ of a helix formed at $T < T_C$.

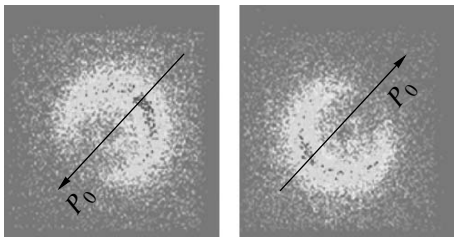

Fig. 3. Patterns of polarized neutron scattering on chiral critical fluctuations in MnSi at $T = T_C + 0.3$ K. The arrow indicates the direction of the initial neutron polarization P_0.

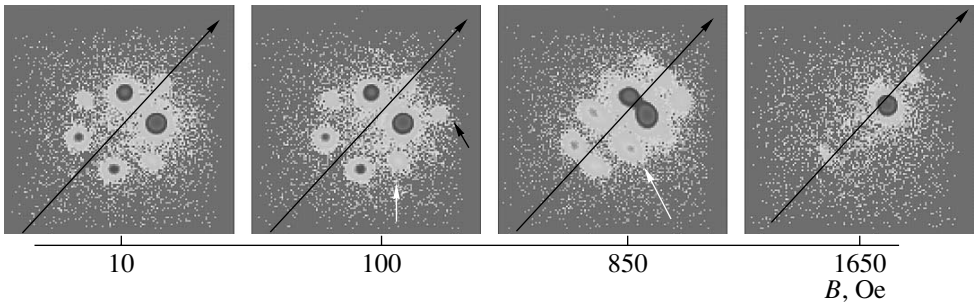

Fig. 4. Evolution of the pattern of polarized neutron scattering on MnSi helices depending on the magnetic field. Long arrows show the direction of magnetic field; white arrows indicate the double scattering peaks; black arrows indicate the second-order reflection peaks.

(ii) At $T < T_C$, four principal diffraction peaks are observed for $\pm\mathbf{q}_1$ and $\pm\mathbf{q}_2$, which correspond to the [111] and $[11\bar{1}]$ directions (Fig. 4); four peaks of double scattering (indicated by the white arrows in Fig. 4); and second-order reflection peaks (indicated by the black arrows).

The second-order reflection peaks appear as a result of the helix deformation caused by a change in the direction of vector **Q**. This behavior is explained by the fact that the helices are aligned in the $\langle 111\rangle$ direction only for $H = 0$, while the application of a magnetic field introduces instability into the helical system. This instability is related to the dependence of the spin wave energy on the angle α between the helix vector **Q** and the magnetic field **H**, which was theoretically expressed as $\varepsilon_q^2(H_\perp) = \varepsilon_q^2 + \Delta^2 - h_\perp^2\cos^2\alpha$, where $h_\perp = g\mu H_\perp$, $H_\perp$ is the field component perpendicular to **Q**. According to this formula $\varepsilon_q^2(H_\perp)$, the energy of spin waves for $H_\perp$ is negative and the energy balance leads to the rotation of **Q** toward the direction of field **H**. As a result, $H_\perp$ decreases and (for **H** ~ 1.3–1.5 kOe), vector **Q** becomes parallel to **H**. Figure 5 illustrates this rotation of helices from the [111] and $[11\bar{1}]$ directions toward *H*.

(iii) The helical structure exhibits a transition to the ferromagnetic state at $H_C = 6.0$ kOe (for **H** || [111]).

(iv) The temperature dependence of the helix pitch can be described as $d(T) = d_0[1 - b(T/T_C)^x]$, where $d_0 = 182 \pm 1$ Å, $b = 0.10 \pm 0.01$, and $x = 2.32$ Å 0.01.

(v) The spin-wave stiffness can be described as $D(T) = D_0[1 - c(T/T_C)^z]$, where $D_0 = 50$ meV Å^2, $c = 0.035 \pm 0.006$, and $z = 2.4 \pm 0.1$. This behavior agrees with the published data for a triaxial spectrometer. It should be emphasized that our data were obtained from a comparison of the magnetic field energy to the spin-weave energy, without energy analysis of scattered neutrons.

(vi) The critical chiral exponent is evaluated at $\beta_c = 0.47 \pm 0.02$, in agreement with the calculations of Kawamura [12]. This value was obtained from the temperature dependence of the chiral intensity $\Delta I(q) = I(q, P_0) - I(q, P_0)$.

Thus, in addition to the validity of Kawamura's hypothesis concerning the new chiral class of universality in second-order phase transitions, which was previously established for a triangular-lattice antiferromagnet [13], we have also corroborated this hypothesis for a helical magnetic MnSi crystal.

3.2. Theory of Helical Magnets

Simultaneously with the realization of experiments described above, Maleyev et al. have developed a theory describing the properties of cubic helical magnetic crystals featuring DM interaction [16]. The theory took into account the following interactions: (i) usual isotropic exchange $J_0 + Dk^2$; DM interaction (D_{DM}); anisotropic exchange (F); dipole interaction (ω_0); Zeeman interaction ($g\mu_B H$); and cubic anisotropy (K). The

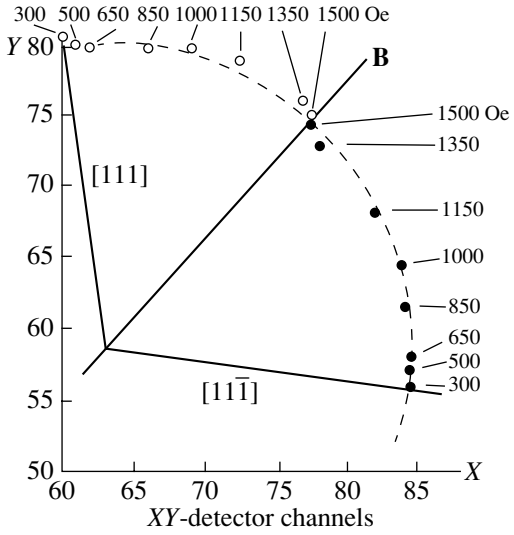

Fig. 5. Rotation of the helix vector **Q** from the initial orientation parallel to the $\langle 111\rangle$ axis to the magnetic field direction (according to the patterns in Fig. 4); *X* and *Y* are the numbers of detector channels.

ground-state energy and the spin-wave spectrum were calculated taking into account that the DM and EX interactions represent first- and second-order spin–orbit interactions. Thus, the hierarchy of interactions in the system under consideration is as follows: $D > D_{DM} > F$, K, ω_0.

Consider a system of coordinates based on mutually perpendicular unit vectors **a**, **b**, **c**. Let spins in the system under consideration be ordered in a helix with wave vector **k** aligned in the direction of the **c** axis. An external magnetic field **H** applied in an arbitrary direction can magnetize the system, causing spins to deviate by an angle α from the plane of helix rotation. The classical ground-state energy of the magnetic system under consideration can be expressed as [16]

$$\begin{aligned} E_{cl} &= -S^2/2(J_0\sin^2\alpha + J_{\mathbf{k}}\cos^2\alpha + \omega_0/3) \\ &\quad - S^2 D_{DMk}(\mathbf{k}[\mathbf{a}\times\mathbf{b}])\cos^2\alpha \\ &\quad + (S^2F/4)[k_x^2(a_x^2 + b_x^2) + k_y^2(a_y^2 + b_y^2) \\ &\quad + k_z^2(a_z^2 + b_z^2)]\cos^2\alpha + Sh_{\parallel}\sin\alpha + (S^2/2)\omega_0 N_{cc}\sin^2\alpha, \end{aligned} \tag{2}$$

where the angle α is determined from the expressions $\sin\alpha \cong -h_{\parallel}/H_c$ for $H < H_c$ and $\sin\alpha = -1$ for $H > H_{c2}$ (H_{c2} being the critical field for the transition from the conical to the ferromagnetic phase); $\omega_0 = 4\pi(g\mu_B)^2/v_0$ is the characteristic energy of dipole interaction; N_{cc} is the demagnetizing tensor component; $h_{\parallel} = g\mu H_{\parallel}$; and $H_{\parallel}$ is the field component parallel to axis **c**. It should be emphasized that, while the classical energy depends on the field parallel to **c**, the system is highly sensitive to a magnetic field component perpendicular to **c**. This is a quantum effect, which will be considered below.

For small **k**, expression (2) can be rewritten as

$$\begin{aligned} E_{cl} &= -(S^2/2(J_0 + \omega_0/3) + [(SDk^2/2) + (S^2FI/4) \\ &\quad - S^2 D_{DM}(\mathbf{k}[\mathbf{a}\times\mathbf{b}])]\cos^2\alpha \\ &\quad + Sh_{\parallel}\sin\alpha + (S^2/2)\omega_0 N_{cc}\sin^2\alpha, \end{aligned} \tag{3}$$

where $I = \Sigma k_\nu^2(a_\nu^2 + b_\nu^2)$ is a cubic invariant, and we obtain the following equation for vector **k**:

$$DK^2 + (SF/2)I(\mathbf{k}) = SD_{DM}(\mathbf{k}[\mathbf{a}\times\mathbf{b}]). \tag{4}$$

As can be seen, the energy E_{cl} is minimum for

$$\mathbf{k} = (SD_{DM}[\mathbf{a}\times\mathbf{b}])/(D + SFI/2). \tag{5}$$

In this case, the spins rotate in a plane perpendicular to vector **k** and the sign of D_{DM} determines the helix type, which is right-handed for a positive D_{DM} and left-handed for a negative D_{DM} (as in MnSi). However, the direction of the wave vector is determined by the sign of F and by the magnitude of the cubic invariant I. In the case of $F < 0$, the energy E_{cl} is at minimum for the maximum absolute value of this invariant, $I = 2k^2/3$; for $F > 0$, the energy E_{cl} is at minimum when the cubic invariant is minimum ($I = 0$). In the former case, vector **k** is directed along the $\langle 111\rangle$ cube diagonal (as in MnSi), while in the latter case, **k** is oriented along the edge of the cube.

The critical field is determined in terms of the main energy interactions in the system under consideration:

$$g\mu_B H_{c2} = h_c = Dk^2 + SFk^2/3 \cong Dk^2. \tag{6}$$

The second term on the right-hand side of Eq. (6) can be ignored, since $D \gg F$. Using relations (5) and (6), it is possible to evaluate the main parameters of the magnetic system such as the spin-wave stiffness $D \cong h_c/k^2$ and the constant $D_{DM} = h_c/k$.

If the magnetic field is applied at an angle to the helix wave vector (so that $h < h_c$), the field-dependent part of the ground-state energy is given by the formula

$$\begin{aligned} E_h &= -Sh_{\parallel}^2/2h_c - Sh_{\perp}^2\Delta^2/\{2h_c(1 + \cos^2\alpha) \\ &\quad \times [\Delta^2 - (h_{\perp}^2/2)\cos^4\alpha]\}. \end{aligned} \tag{7}$$

where $h_{\parallel}$ and $h_{\perp}$ are the components of the magnetic field **h** parallel and perpendicular, respectively, to vector **k**. The first term on the right-hand side of Eq. (7) is the magnetic part of the classical energy considered above. The second term describes the interaction of the helix with the field component perpendicular to the helix wave vector. This term, having a quantum character, is responsible for the rotation of the helix wave vector toward the magnetic field vector, which was observed in our experiments [15]. The theory predicts the presence of a spin-wave gap Δ in the second term, otherwise the magnetic system will be unstable with respect to a negligibly small field perpendicular to vector **k**. It should also be noted that the magnetic field component perpendicular to the helix wave vector produces deformation of the helix structure, which leads to the appearance of higher harmonics. The corresponding second-order reflections were observed in our experiments [15] and previously reported by Lebech et al. [17].

In accordance with the theory, it is possible to determine the part of the ground-state energy (E_h) that is responsible for interaction with the magnetic field and to express it as a function of angles ϑ and φ, which relate the basis set **a**, **b**, **c** to the coordinate system of the crystallographic cell for various values of Δ. In these coordinates, the 2D ground-state energy surface has minima at $\vartheta = \arccos(1/\sqrt{3})$ and $\varphi = \pi/4$, which correspond to the [111] axis, which is parallel to the direction of the field. As the applied field is increased up to $h = \Delta$, a new trough appears on the energy surface. This trough, being aligned in the direction perpendicular to the field, implies the appearance of a new minimum. However, the trough is too shallow in comparison to the minimum related to the field component parallel to the [111] axis. The trough becomes deeper than the minimum along the [111] axis when $\Delta < h < \Delta\sqrt{2}$. There-

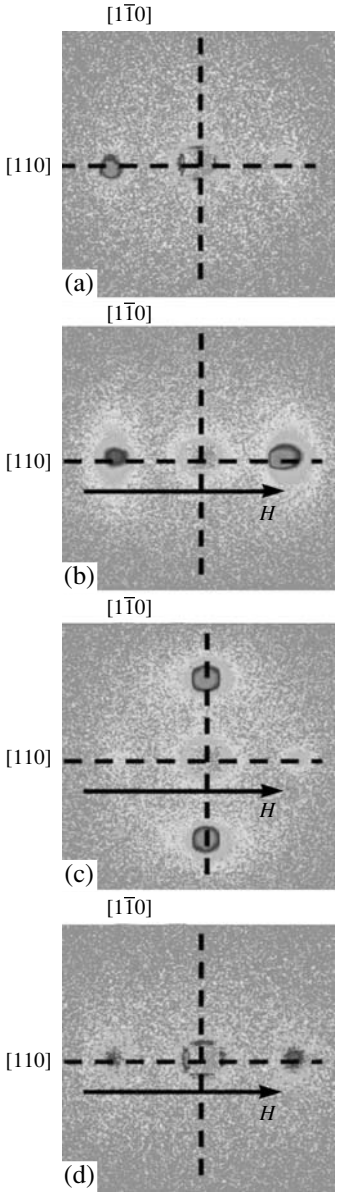

Fig. 6. Reorientation of the helix vector from the initial [1$\bar{1}$1] direction (parallel to the field) to a perpendicular [1$\bar{1}$0] direction in a field between 70 and 150 mT: (a) H = 0; (b) H = 70 mT; (c) $H \approx 0$ = 150 mT; (d) H = 250 mT.

fore, in this interval of fields, one can expect that vector **k** will rotate from the [111] axis (field direction) to a perpendicular direction. This implies the possibility of observing a phenomenon related to the chiral quantum phase transition in experiment.

3.3. Chirality of MnSi: Second Stage of Investigation

In order to check for theoretical predictions concerning a 90° reorientation of vector **k**, we have performed a special experiment [18] with a sample crystal and a magnetic field **H** oriented so as to observe simultaneously the two Bragg reflections related to the orientations of vector **k** parallel to the mutually perpendicular directions [111] and [1$\bar{1}$0]. The primary polarized neutron beam was directed along the [11$\bar{2}$] axis (i.e., it was perpendicular to both [111] and [1$\bar{1}$0] directions. In the case of polarized neutron scattering on a magnetic helix with a large pitch, this experimental geometry allows the two diffraction peaks to be observed in the region of small scattering angles, provided that the Bragg condition is satisfied. Although the Bragg condition in the ideal system can be satisfied for only one satellite, both these peaks have been observed (Fig. 6) due to a high mosaicity of the magnetic structure.

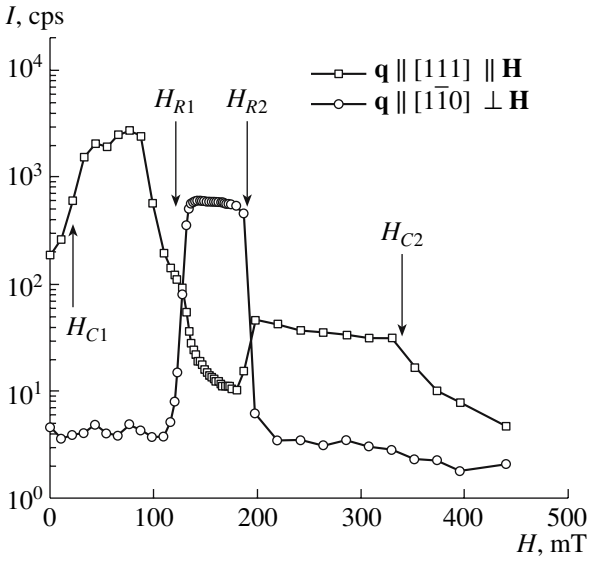

Fig. 7. The field dependence of the intensity I of polarized neutron scattering related to the magnetic helices oriented in the [111] and [1$\bar{1}$0] directions.

Figure 7 shows the field dependence of the intensity of peaks related to the magnetic helices oriented in the [111] and [1$\bar{1}$0] directions. As can be seen, the intensity due to the [111] helix grows when H increases from 0 to 80 mT. This pattern reflects the rotation of all possible helix directions toward the field H (i.e., to the [111] axis). Then, the intensity of this peak drops, while the intensity of a peak related to the perpendicular helix [1$\bar{1}$0] grows and then remains constant in the interval from H_{R1} to $-H_{R2}$ (centered at H = 160 mT). This corresponds exactly to reorientation of the helix by 90° (perpendicularly to **H**), predicted theoretically in the form of a trough with a minimum on the potential surface, where $h_1 \approx \Delta\sqrt{2}$ and the spin system loses stability. The patterns of reflections observed for H = 0. 70, 150, 250 mT in Fig. 6 reveal this reorientation by a 90° change in the helix vector direction for H between 70 and 150 mT.

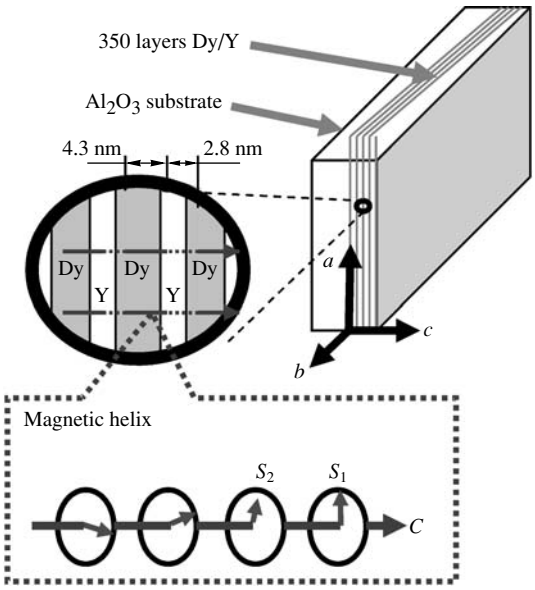

Fig. 8. Schematic diagram of a Dy/Y multilayer structure with the helix wave vector directed along the *c* axis.

The theoretical prediction of a gap in the spin-wave spectrum, as well as the experimental observation of instability related to this gap in the spin system, confirm the conclusions of Pfleiderer et al. [19–21] that MnSi features a quantum phase transition to a disordered state, which is achieved under hydrostatic pressure. It was demonstrated [19–21] that T_C decreased with increasing pressure, and the magnetic order disappeared at $T \approx 0$ and a critical pressure of $P_c \approx 14.6$ kbar. However, the nature of the spin instability remained unclear. Our results contribute significantly to the elucidation of this nature. Under hydrostatic pressure, all the aforementioned interactions are altered, which can lead to spin melting. In order to check for this possibility, we are planning to continue these investigations with polarized neutrons on MnSi crystals under pressure.

4. CHIRALITY OF THE Dy/Y SYSTEM

Another interesting experiment [22] has been carried out on a Dy/Y multilayer system, which is known to possess a helical spin structure. The aim of this experiment was to check whether this system has an average chirality, that is, a difference in populations of the left-handed (n_L) and right-handed (n_R) helices, which is necessary for determining chiral exponents. It should be noted that such investigations could be performed only using polarized neutron scattering.

The sample was a superlattice similar to that used by Erwin et al. [23], comprising a sequence of Y(50 nm)[Dy(4.3 nm)//Y(2.8 nm)]$_{350}$/Y(234 nm)/Nb(200 nm) layers on an Al_2O_3 substrate, which was created by the method of molecular beam epitaxy. The layers were grown on the plane perpendicular to the [001] axis of the hexagonal Dy/Y structure (a quasi-single crystal). The multilayer plate had dimensions of 60×60 mm.

The magnetic properties of bulk dysprosium are well known [24]: below the Néel critical temperature ($T_N = 180$ K), the spin system of a Dy/Y crystal (possessing a hexagonal structure) is ferromagnetically ordered in the **ab** plane, but the spins are curled along the **c** axis into a helix that is incommensurate with the crystal structure. As the temperature decreases, the helix pitch increases from 2.5 to 4.0 nm. Below the Curie temperature $T_C = 89$ K, the system exhibits a transition to the ferromagnetic state.

The situation for Dy/Y superlattices is similar to that for bulk dysprosium because Y can be considered as a nonmagnetic analog of Dy. Below $T_N = 166$ K, a coherent spin helix with a characteristic coherence length much greater than the thickness of the Dy/Y double layer appears, whereas the ferromagnetic transition at $T_C = 89$ K is suppressed [23]. It is suggested that the coherent spin helix penetrates through paramagnetic Y layers due to the Ruderman–Kittel–Kosuya–Iosida (RKKY) interaction, although direct evidence is lacking. It can also be suggested that a 1.6% lattice misfit between bulk Y and Dy leads to epitaxial tension in the Dy (and Y) lattice, which gives rise to stresses in the direction perpendicular to the plane of layers. It is assumed that stresses that develop in the Dy lattice are capable of creating a difference in the populations of left- and right-handed helices as described in [25]. As will be shown below, such a difference between n_L and n_R was in fact observed in our experiment [22].

The experiment was performed on the same setup for small-angle neutron scattering as that used to study the chirality of MnSi, but the measurements were performed in the reflection mode in a range of momentum transfer q from 6×10^{-2} to 3 nm^{-1}. The scattering intensity was measured at temperatures from 30 to 190 K for different signs of the initial polarization $\mathbf{P}_0$. The external magnetic field up to 10 mT was perpendicular to the incident beam and parallel to the **c** axis of the sample (Fig. 8). In contrast to the case of MnSi, where all helices were of the same handedness, in the Dy/Y system it was important to thoroughly measure the relative difference $(n_L - n_R)/(n_L + n_R)$, that is, the ratio of the difference $\Delta I(P_0) = I(+P_0) - I(-P_0)$ to the sum $\Sigma I(P_0) = I(+P_0) + I(-P_0)$, which can be called the polarization of the reflection: $P_s = \Delta I(P_0)/\Sigma I(P_0)$. The angular position of the reflection on the neutron scattering map (Fig. 9) was used to determine the wave vector transfer $2\pi/d$, where d is the period of the structure.

Figure 9a presents a map of the diffraction peaks (on a logarithmic scale) at $T = 150$ K, and Fig. 9b shows the scattering intensity variation in a horizontal q_x scan. The two symmetric peaks (denoted NL and NR on the left- and right-hand sides, respectively) closest to the center ($q = 0$) are due to reflections from the nuclear

periodic structure. Neither positions nor intensities of these peaks change in the entire temperature range studied, and they have $P_S = 0$. The most intense peak (denoted MR) on the right side of the map is due to the scattering from the spin helix. This peak appears below $T = 166$ K. As the temperature is decreased to 100 K, the helix pitch increases from 2.34 to 2.78 nm and remains constant at $T < 100$ K. A peak between NR and MR appears as a result of the modulation of the magnetic helix by the nuclear layer structure and is denoted ModR. Both MR and ModR peaks are characterized by positive P_S values.

The parameters of the MR reflection have been quantitatively processed. As can be seen from the neutron scattering cross section S for a helical structure [14], the polarization-independent part of the scattering intensity $\Sigma I(P_0)$ is proportional to S^2, while the **P**-dependent part is proportional to the mean chirality $\langle \mathbf{C} \rangle = \langle [\mathbf{S}_1 \times \mathbf{S}_2] \rangle$. It was established that a spontaneous chirality on a level of 7–8% appeared at $T < T_N$. Thermal cycling in a zero magnetic field did not change the magnitude and the sign of the spontaneous chirality. The results of experiments with a magnetic field applied along the helix vector showed the presence of a field-induced difference in the populations, $(n_L - n_R)/(n_L + n_R)$, which was dependent both on the field magnitude and on the temperature. The P_S value reached 25% in magnetic fields on the order of 1 T. The temperature dependence of the total intensity $\Sigma I(P_0)$ was fitted to a scaling expression as $\Sigma I(P_0) = I_0 \tau^{2\beta}$ for $\tau < 0.1$, where $\tau = (T_N - T)/T_N$, and β is the critical magnetization exponent. It was found that $T_N = 165.3 \pm 0.2$ K and $\beta = 0.40 \pm 0.01$, which coincided with the β value for pure dysprosium [24]. Assuming that the mean chirality varies with the temperature as τ^{β_c}, the behavior of the magnetic reflection polarization P_S can be described as $P_S \sim \tau^{\beta_c - 2\beta}$. In the critical region, this fitting yields $T_N = 165.4 \pm 0.2$ K and $\beta_c - 2\beta = 0.22 \pm 0.01$, which corresponds to $\beta_c = 1.02 \pm 0.2$. Note that $\beta_c \sim 1$ is close to the exponent $\beta_c = 0.90(3)$ reported for holmium [25], where a difference in the populations n_L–n_R was artificially created by torsional straining. By analogy with [25], one can assume that a mechanism of interlayer straining stresses is operative in the Dy/Y multilayer system, which is related to a 1.6% misfit between Dy and Y crystal lattices.

In concluding, the experiment described in this section revealed for the first time the mean chirality in the Dy/Y layer system with a critical exponent of $\beta_c = 1.02 \pm 0.2$.

5. SPIN DYNAMICS IN Fe–Ni INVAR-TYPE ALLOYS

An important property of polarized neutrons is their increased sensitivity to magnetic inhomogeneities,

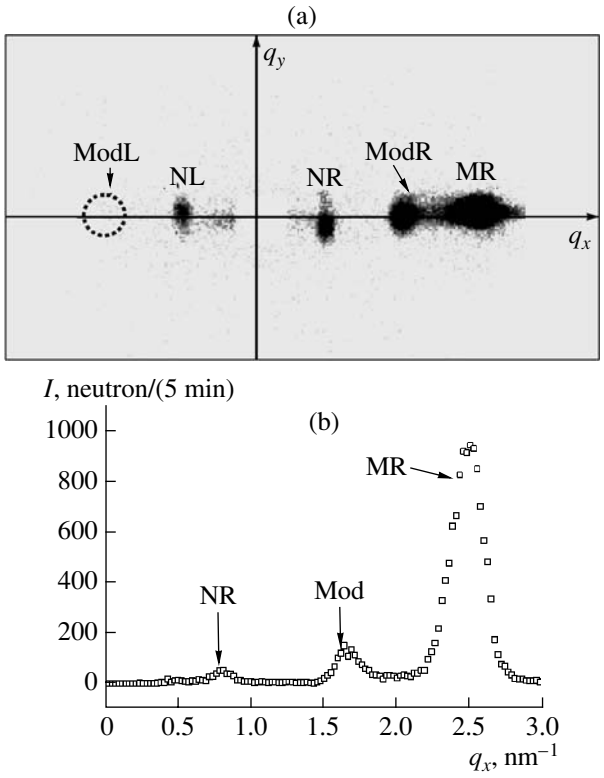

Fig. 9. Neutron reflections from a Dy/Y layered structure: (a) a pattern observed on the *XY* plane of the detector; (b) a cross section of the reflections along the q_x axis (MR is a Bragg reflection from the spin helix).

which is due to the nuclear-magnetic interference in the coherent wave scattering. Indeed, the amplitude a_m of the magnetic scattering of neutrons depends on the polarization **P** as $a_m = R\mathbf{M}_\perp\mathbf{P}$ (where R is a constant coefficient), while the nuclear scattering amplitude a_n is polarization-independent. As a result of interference, the a_m and a_n amplitudes are added ($a = a_n + a_m$) and the differential cross section acquires the following form: $d\sigma/d\Omega = a_n^2 + 2a_n a_m(\pm P_0) + a_m^2$. Then, the difference of scattering intensities is $\Delta I(q, P_0) = I(q, P_0) - I(q, P_0) = 4a_n a_m$. This value is at least two times as large as the intensity of scattering for unpolarized neutrons, for which $d\sigma/d\Omega = a_n^2 + a_m^2$. The difference in the results of two measurements with variation of only one parameter P_0 eliminates the entire polarization-independent background.

The use of a nuclear-magnetic interference in the critical small-angle scattering of polarized neutrons on a $Fe_{65}Ni_{35}$ (Invar) alloy in a paramagnetic state near $T_C = 485$ K gave rather unexpected results [26]. The interference scattering caused by the spin–lattice interaction revealed a correlation between the critical magnetization fluctuations and the nuclear density fluctuations. The magnetic scattering in this system was iden-

tified as the scattering on critical fluctuations. At the same time, the dependence of the interference scattering on the momentum transfer q showed that the form factor of nuclear scattering is identical to the magnetic form factor. From this, it was concluded that the form and the lifetime of a nuclear object are correlated and limited by the form and the lifetime of critical magnetic fluctuations. It was also established that the relative local variation of the lattice reaches $\Delta d/d \sim 0.004$. The characteristic size of the region of lattice deformation is on the order of 5.0–7.0 nm, depending on the temperature and the magnetic field.

Thus, we have established for the first tine a rigid relation between the atomic magnetic moments and the lattice in the paramagnetic region, where the Invar effect does not operate on the macroscopic scale (ferromagnetic fluctuations at $T > T_C$ c are also of the Invar type). This result leads to a new point of view on the nature of Invar-type alloys. Brown [27] demonstrated that the magnetic moments of Fe and Ni do not vary with temperature in a broad range, which implies that the atomic magnetic moments keep the lattice unchanged in this temperature range by means of strong spin–orbit coupling. This hypothesis requires theoretical verification, but it has the right to exist along with other hypotheses on Invar mechanisms.

The discussion about a 1.5- to 2-fold difference between the magnetic stiffness (D_n) determined by neutron methods and the values (D_m) calculated from magnetization measurements in Invar-type alloys was based on the results of neutron measurements for relatively large q and $\omega \geq 1$ meV, and it was suggested that this difference might vanish for a small energy transfer ω. However, our experiments [1] with $Fe_{65}Ni_{35}$ showed that this difference also takes place at small q and ω = 10–100 μeV.

According to Bloch's model, the temperature dependence of the saturation magnetization M_s can be described by the formula

$$M_s(T) = M_s(0)(1 - BT^{3/2}), \quad (8)$$

where $B = [2.612g\mu_B/M_s(0)](k_B/4\pi D)^{3/2}$, k_B is the Boltzmann constant, and D is the spin-wave stiffness, defined for Heisenberg ferromagnets as $D(T) = D_0(1 - AT^{5/2})$. The magnetic measurements of M_s can be used to determine $D_n(T)$ and measurements of D by the method of magnetic scattering of neutrons can be used to obtain D_n. According to the results of numerous experiments, D_m and D_n values coincide well for ferromagnetic materials except for Invar-type alloys, where the saturation magnetization M_s decreases faster with increasing temperature than might be expected from $D_n(T)$ calculations. In order to provide for the experimental value of $M_s(0)$, $D_m(0)$ must be on the order of 80 meV Å^2, whereas the neutron data give $D_n(0) \sim 140$–190 meV Å^2 [28, 29]. The hypothesis of additional "latent" spin-wave excitations, which was formulated in order to explain the discrepancy, has found no experimental evidence.

Another hypothesis consists in the sample magnetization being measured at $q = 0$, in the state of which the long-wave spin-wave excitations are suppressed by the dipole–dipole interaction, whereas the neutron scattering is measured for q that exceeds the dipole momentum q_d. In fact, it would be correct to compare $D_m(q = 0)$ to $D_n(q \sim 0)$. We have performed such measurements on the aforementioned setup for small-angle polarized neutron scattering at GKSS (Geesthacht, Germany). The measurements were performed in the oblique geometry developed previously, which allowed the antisymmetric part of magnetic scattering (related to the dynamic three-spin correlations) to be determined in a magnetic field oriented at an angle (optimum, 45°) relative to the direction of the incident neutron beam. The result is extracted from the LPA data and represents pure dynamic scattering on spin-wave excitations in the range of small q and ω.

The first measurements using this scheme were performed in the interval from T_C = 485 K to 300 K, and the results were extrapolated to $T = 0$ according to the commonly accepted law $D(T) = D(0)(1 - T^{5/2})$, which follows from the Bloch equation (8). The experiment [11] yielded $D_n(0) = 117 \pm 2$ meV Å^2, which was smaller than the values for large q and ω, but still greater than $D_m(0)$. However, it was established in subsequent experiments that this result suffered from the ambiguity of data interpolation to $T = 0$ from the far range of $T > 300$ K.

The measurements were continued on a sample of $Fe_{65}Ni_{35}$ with T_C = 485 K in a temperature range from 50 to 500 K and an external field varied within 70–250 mT. It was found that, in the entire temperature range studied, $0.9 > \tau = (1 - T/T_C) > 0.1$, the behavior of $D_n(\tau)$ is reliably described by the power law $D(\tau) = D_0\tau^x$ with $x = 0.48 \pm 0.01$ and $D_0 = 137$ meV Å^2, which coincides with D_n determined using a triaxial spectrometer [29] (Fig. 10). The spin-wave damping behaved as $\Gamma_q = \Gamma_0 q^2$ with $\Gamma_0 = 12$ meV Å^{-2} in the entire range $0.9 > \tau > 0.1$. In other words, the experiment showed that the $T^{5/2}$ law following from Bloch equation (8) was completely invalid for Invar-type alloys.

It should be noted that the observed temperature dependence, $D(\tau) = D_0\tau^x$, which is valid in a broad temperature range, indicates that this entire temperature interval is critical. We can naturally assume that, in fact, the Invar system occurs in a critical region with respect to parameter G (pressure). Indeed, experiments with variable pressure [30, 31] showed a sharp decrease in T_C with increasing pressure, up to $T_C \approx 0$ at a critical pressure of G_c = 6 GPa. With decreasing temperature, the balance of the spin–orbit coupling and other interactions can give rise to elastic stresses and internal pressure, which is equivalent to external loading.

Accordingly, at a temperature of $T_x < T_C$, the system occurs in a critical region at T_{CGx}, determined by the induced internal pressure ($T_{CGx} < T_C$). In this case, the temperature $T = 0$ corresponds to a quantum critical point. The proposed pressure mechanism explains the sharp decrease in T_C with increasing Fe content in Fe–Ni alloys, from $T_C = 600$ K in $Fe_{60}Ni_{40}$ to $T_C = 0$ in $Fe_{75}Ni_{25}$ [e32]. Note that, in this case, the internal pressure can additionally vary due to a misfit between Fe and Ni lattice parameters.

6. MAGNETIC SHAPE MEMORY EFFECT

Materials featuring thermoelastic martensite transitions, which ensure a reversible plastic deformation called the shape memory effect, have attract the attention of researchers for several decades. This interest is related primarily to practical applications of such materials in aerospace technologies, medicine, and high-precision machine building. Alloys exhibiting memory effect belong to so-called functional materials, the properties of which can be effectively controlled by changing external parameters. In recent decades, a new direction in the development of functional materials has appeared, which deals with the magnetically controlled shape memory (MSM) effect. The most typical representative of these materials is the Heusler alloy.

The Heusler alloy is a ternary intermetallic alloy of Ni_2MnGa composition, which exhibits the martensite transition from a cubic $L2_1$ type phase to a tetragonal phase with a ratio of unit cell parameters of $c/a = 0.94$. A special feature of this alloy is that the martensite transformation takes place in the ferromagnetic state; the ferromagnetic transition temperature T_C and especially the martensite transition temperature T_m change significantly when the alloy composition deviates from stoichiometry. The strong relationship between the structural and magnetic subsystems accounts for the attractive properties of these alloys, such as the MSM effect, which reaches 6% in some alloys of the Ni–Mn–Ga system. These materials also have a significant advantage in the rate at which they respond to a change in the control parameters. Numerous macroscopic and neutron scattering investigations have been performed in order to elucidate the nature of the MSM phenomenon [33, 34]. Both the usual shape memory effect and the MSM are substantially influenced by deviations in the alloy's composition from stoichiometry, which must be also accompanied by fluctuations in the nuclear and spin density as manifested by the small-angle neutron scattering. The structural fluctuations proper could hardly be observed in Ni_2MnGa, because the change in the unit cell volume upon the martensite transition from a cubic to a tetragonal phase is very small (below 1%), but this alloy exhibits a unique situation in which fluctuations (or nuclei of the new phase) appearing during the structural phase transition can be observed due to magnetic contrast. Our investigations demonstrated

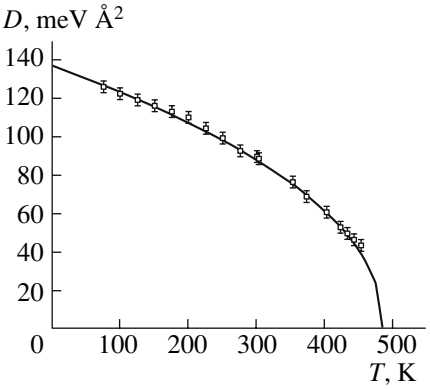

Fig. 10. The temperature dependence of the magnetic stiffness $D(T)$ of a $Fe_{65}Ni_{35}$ alloy. Points present the experimental data [29], the solid curve shows the results of calculations using the $D = D_0\tau^x$ formula.

that the experimentally observed small-angle neutron scattering and the magnetic-nuclear interference involved in the scattering can be explained in terms of the magnetic decoration of tetragonal domains formed in the first-order phase transition, which possess a magnetic moment significantly different from that of the cubic phase.

The goal of our recent experiments [35] was a comparative study of the evolutions of the mesoscopic structure (mesostructure) in the stoichiometric (Ni_2MnGa) and nonstoichiometric ($Ni_{49.1}Mn_{29.4}Ga_{21.5}$) alloys in a broad temperature range ($15 < T < 400$ K).

Figure 11 presents comparative data for the stoichiometric (S) and nonstoichiometric (NS) systems, which reveals a significant difference in the temperature-dependent evolution of the mesostructure. As is known, the two materials also exhibit different MSM characteristics: as a rule, a significant MSM effect is observed only in NS compositions (in the $Ni_{49.1}Mn_{29.4}Ga_{21.5}$ alloy under consideration, this effect amounted to 2.5%). Both alloys exhibited virtually the same Curie temperature ($T_C \cong 373$ K), whereas the martensite transition temperatures differed by 90 K: $T_m = 306$ K (NS) against 216 K (S). These values of T_m coincide with the published data, but the evolution of the mesostructure in the vicinity of T_m revealed several specific features. The main distinctions in the intensity of small-angle neutron scattering in the NS and S compositions were as follows:

(i) An increase in the scattering intensity with decreasing temperature in the austenite phase on the NS composition (for $T_m < T < T_C$) and a sharp drop (i.e., nearly complete homogenization of the alloy on the mesoscopic scale) at $T \approx T_m$ upon the transition to the martensite phase, in contrast to a jump in the scattering intensity in the martensite phase of the S composition.

(ii) An increase in the intensity of scattering in the martensite phase of the NS composition at $T < 150$ K.

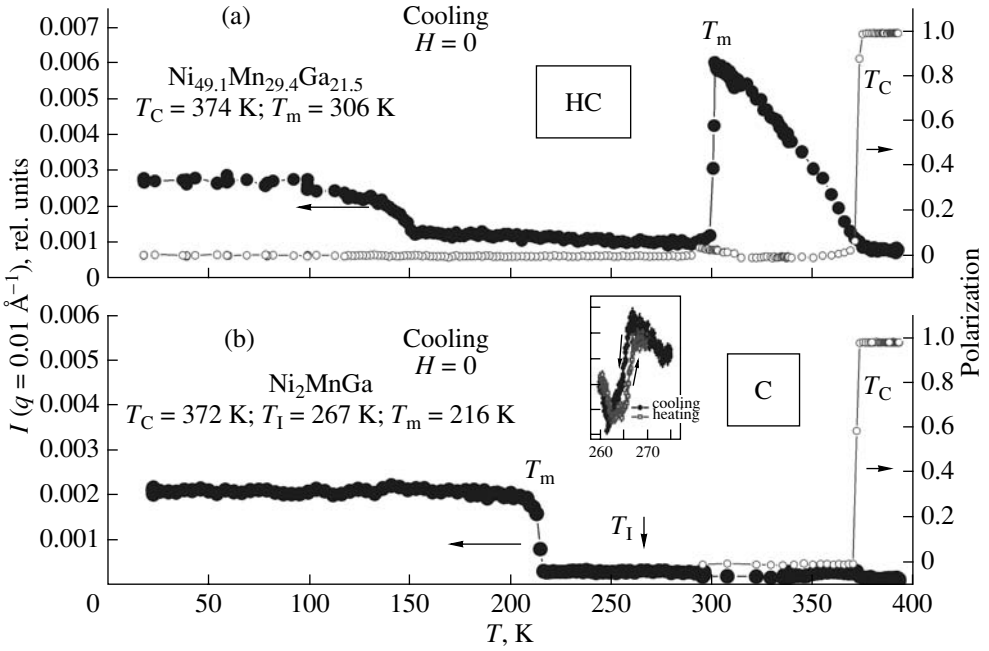

Fig. 11. Comparative data on the temperature evolution of mesoscopic inhomogeneities in zero-field-cooled samples of Ni_2MnGa alloy with (a) nonstoichiometric and (b) stoichiometric composition. The inset in (b) shows the scattering peak corresponding to a pre-martensite phase transition at T = 267 K on a greater scale.

(iii) A peak in the intensity of scattering in Ni_2MnGa at $T_I \approx 267$ K (see the inset to Fig. 11b), which has been explicitly recorded for the first time and interpreted as a reflecting premartensite phase transition.

The observed behavior of the mesophase in c requires theoretical interpretation. The method of small-angle scattering of polarized neutrons proved once again to be an effective tool for detailed investigation of the mesostructure—an important factor determining the properties of functional materials.

7. SELF-ORGANIZATION OF MAGNETIC NANOPARTICLES IN A LIQUID MATRIX

Investigations of ferrofluids is important both from the standpoint of deeper insight into the basic features of supermagnetism and for the practical use of magnetic fluids (MFs) in various applications, including high-density data recording media, targeted drug delivery systems in medicine, magnetic slide bearings, vacuum-sealed mobile joints, and many others.

An MF is a stable system exhibiting no phase separation, representing a solution of magnetic monodomain nanoparticles in a nonmagnetic liquid solvent (water, kerosene, or other organic fluids.). Nanoparticles can be protected against coagulation by a layer of surfactants (typically, fatty acids or their salts). The stability of MFs is ensured by a fine balance of forces acting upon these particles, including dipole–dipole forces, van der Waals forces, gravity, etc. On the other hand, this is a system without a clearly pronounced ground state, since the dipole interactions lead to strong correlations among the rotational and translational degrees of freedom. As a result, certain particle concentrations allow fluctuations both in their number density and magnetization even in the absence of external magnetic field. Ferromagnetic particles in MFs can also exhibit self-organization phenomena. In our experiments [36], self-organization was observed in a near-bottom layer of an MF in a cell. These neutron experiments were performed on an EVA reflectometer at the Laue–Langevin Institute (Grenoble, France).

Figure 12 shows diagrams of ferrofluids based on Fe_3O_4 nanoparticles with concentrations of c = 2, 5, and 7% in heavy water (D_2O). A narrow (sheet) beam of neutrons was incident on a silicon cell from below, transmitted through the bottom, and scattered from a near-bottom layer of the ferrofluid. The results of processing the scattering data as a function of q showed stratification after 10–20 h of exposure in a zero magnetic field. The number of layers rapidly increased with increasing concentration c of magnetic particles. Ferrofluids with $c \geq 7\%$ exhibited a Bragg peak of scattering from a volume quasi-crystal. The application of an external magnetic field with $H_{\parallel}$ up to 10 mT parallel to the bottom of the cell had little effect on the process of self-structurization in the ferrofluid with c = 2–6%. At a greater concentration, the number of layers significantly increased with $H_{\parallel}$. The application of an orthogonal field $H_{\perp}$ led to densification of the layers, up to the formation of a close-packed hexagonal structure.

8. HEAVY-FERMION SYSTEM $CeRu_2Si_2$

Investigations into the properties of compounds with heavy fermions (HFs) is among the extensively developing fields of the physics of condensed state in the recent quarter of a century. At temperatures below the Kondo temperature (T_K), the antiferromagnetic interaction between conduction electrons and those localized on a partly occupied *f* shell of a rare-earth ion in HF compounds leads to the so-called coherent Kondo effect. This phenomenon is manifested by the formation of quasi-particle states at the Fermi level, the effective masses m^* of which are two orders of magnitude higher than the free electron mass m_e. Such particles (HFs) have been observed in a large number of compounds, referred to as HF metals.

The main body of information concerning HFs has for the most part been obtained by macroscopic methods (heat capacity and electric resistance measurements, de Haas–van Alfvén effect), which are sensitive to a narrow layer of carriers (with a width on the order of temperature *T*) near the Fermi level. Earlier, neutron experiments were performed in the range of large momentum transfer *q*, where the magnetic scattering is sensitive to the system of localized magnetic moments and provides only indirect information about HFs. However, Maleyev [37] showed that HF quasi-particles in such compounds can be directly observed in polarized neutron scattering measurements, since the orbital part of the magnetic scattering amplitude contains a term singular for $q \longrightarrow 0$. This term accounts for small-angle neutron scattering on mobile charge carriers, the effect being proportional to $(m^*/M)^2$, where *M* is the neutron mass. For common metals, this factor is $(m^*/M)^2 \sim 10^{-5}$–10^{-6}, so that this contribution to scattering is negligibly small. However, in HF compounds with $m^* \sim 100\ m_e$, we have $(m^*/M)^2 \sim 10^{-2}$. In such cases, the neutron–electron scattering component can be detected and the corresponding cross section depends on the scattering angle ϑ as $d\Sigma(\vartheta)/d\Omega \propto \vartheta^{-1}$ for $2E\vartheta \propto T$ and as $\propto\vartheta^{-2}$ for $2E\vartheta \ll T$, where *E* is the neutron energy [37]. A crossover between the two regimes should be observed at $\vartheta_c \cong T/2E$, which is related to the following circumstance: for $2E\vartheta \ll T$, neutrons are scattered on thermally excited quasi-particles, while for $2E\vartheta \gg T$, the temperature is insignificant.

Thus, the small-angle scattering of polarized neutrons can be used to probe a layer with a width of $E\vartheta$ near the Fermi level. This product can be varied within broad limits, which implies that the probe can penetrate deep under the Fermi surface and study the spatial structure of fluctuations of the HF current depending on $E\vartheta$, *T*, and the external magnetic field *H*.

We have studied [38] small-angle scattering of polarized neutrons from a $CeRu_2Si_2$ single crystal for the purpose of direct observation of scattering from HF quasi-particles at low temperatures and the investigation of magnetic field effects. Previously, the $CeRu_2Si_2$ system was characterized by various methods as a typical HF compound with $T_K \approx 25$ K, which does not possess superconducting properties and does not exhibit magnetic phase transitions at low temperatures in the region of $T \approx 1$ K (such transitions would substantially complicate the interpretation of experimental data). Experiments were performed using neutrons with two wavelengths $\lambda = 8.1$ and 10.5 Å (at $\Delta\lambda/\lambda = 10\%$), in the interval of momentum transfer $0.6 \times 10^{-2} < q < 2.1 \times 10^{-1}$ Å^{-1}, in the range of magnetic fields $0 \le H \le 2.5$ T, and at temperatures within $T = 0.85$–1.2 K.

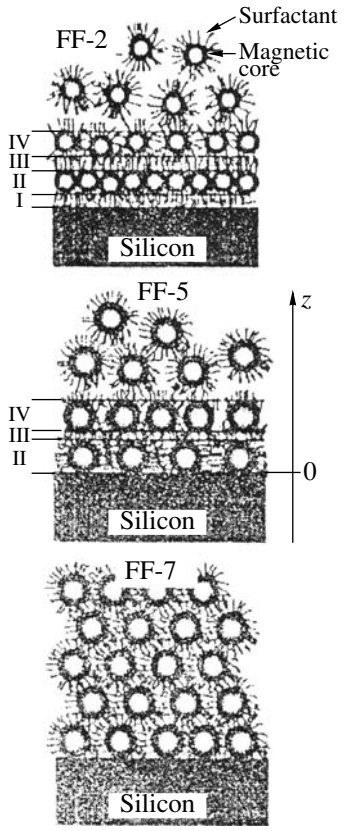

Fig. 12. Diagrams illustrating self-organized structurization in ferromagnetic fluids (FF) comprising Fe_3O_4 nanoparticles with concentrations $C = 2$ (a), 5 (b), and 7% (c) in heavy water (D_2O).

The main experimental results were as follows [38]:

(i) Small-angle neutron scattering was observed at $T = 0.85$ K and $H = 0$ in the range of momentum transfer $q \le 0.04$ Å^{-1}. According to theoretical predictions [37] and our estimates, this scattering could be interpreted as the orbital part of magnetic scattering on HF quasi-particles (Fig. 13).

(ii) The application of a magnetic field *H* (up to 2.5 T) increases both the scattering intensity (Fig. 13) and makes it anisotropic relative to the field direction (Fig. 14). The scattering also depends on the orientation

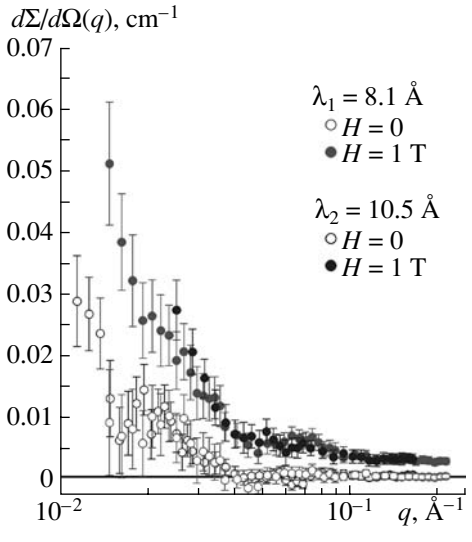

Fig. 13. Small-angle scattering of polarized neutrons on HF system ($CeRu_2Si_2$) at T = 0.85 K for two neutron wavelengths λ = 8.1 Å and λ = 10 Å in magnetic fields H = 0 and 1 T (in the q-scan, there is no difference between λ_1 and λ_2).

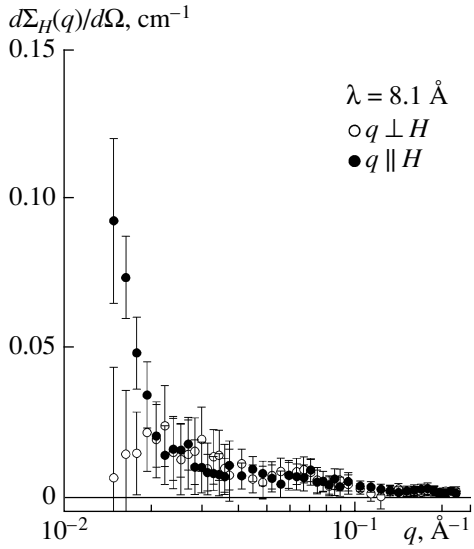

Fig. 14. Small-angle scattering of polarized neutrons on HF system ($CeRu_2Si_2$) at T = 0.85 K for two orientations of the applied magnetic field relative to the direction of the momentum transfer vector **q**.

of $CeRu_2Si_2$ single crystal relative to the incident neutron beam and the magnetic field H.

(iii) Measurements with the applied magnetic field H revealed additional scattering for $q > 0.04$ Å^{-1}, which is well described by a Lorentzian curve and can be interpreted as the magnetic scattering of neutrons on spin density fluctuations with a correlation radius of $R_c \approx 30$ Å.

Thus, we have observed for the first time the small-angle scattering of polarized neutrons on HF quasi-particles. The experiment showed that, using primary neutron beams of higher intensity, it is possible to study the properties of heavy fermions in more detail.

9. CONCLUSIONS

It should be emphasized that all results considered in this paper were obtained only owing to the use of polarized neutrons. Polarized neutrons offer a unique radiation probe for studying magnetism, which is capable of revealing the magnetic phenomena not "seen" by other techniques. We have used well-verified methods developed in our previous work. However, the polarized neutron techniques are continuously developing. In particular, radio-frequency spin-echo techniques have been developed, which allow the spin-echo unit to be miniaturized and incorporated into usual diffractometer and spectrometers, thus increasing their resolution with respect to both q and ω. We believe that such developments will bring absolutely new, unexpected results in the nearest future.

ACKNOWLEDGMENTS

The authors are grateful to the staff of the WWR-M reactor for technical assistance and normal functioning of the reactor, to the scientific administration of the GKSS (Geesthacht (Germany), the Laue–Langevin Institute (Grenoble, France), and the Delft Technological University (Delft, Netherlands) for kindly providing the opportunity to use the small-angle neutron scattering facilities.

These investigations were supported for many years by the Russian Foundation for Basic Research, Presidential Program for Support of Leading Scientific Schools in Russia, Research Programs of the Ministry of Education and Science of the Russian Federation, and Scientific Programs of the Russian Academy of Sciences.

REFERENCES

1. O. Halpern and M. H. Johnson, Phys. Rev. **55**, 898 (1939).
2. S. V. Maleyev, Zh. Eksp. Teor. Fiz. **40**, 1224 (1961) [JETP **40**, 1224 (1961)].
3. A. V. Lazuta, S. V. Maleyev, and B. P. Toperverg, Zh. Eksp. Teor. Fiz. **75**, 764 (1978) [JETP **48**, 386 (1978)].
4. A. I. Okorokov, V. V. Runov, and G. M. Drabkin, "The Method of Determination of Neutron Beam Polarization Degree," The USSR Inventor's Certificate No. 408247, Byull. Izobret. no. 47 (1973).
5. S. V. Maleyev and V. A. Ruban, Zh. Eksp. Teor. Fiz. **62**, 415 (1972) [JETP **35**, 222 (1972)].
6. A. I. Okorokov and V. V. Runov, Physica B **297**, 239 (2001).
7. A. I. Okorokov, A. G. Gukasov, Ya. M. Otchik, **et al.,** Phys. Lett. A **65** (1), 60 (1978).

8. A. V. Lazuta, S. V. Maleyev, and B. P. Toperverg, Zh. Eksp. Teor. Fiz. **81** (4), 1475 (1981) [JETP **54**, 782 (1981)].
9. A. I. Okorokov, A. G. Gukasov, V. V. Runov, et al., Zh. Eksp. Teor. Fiz. **81** (4), 1462 (1981) [JETP **54**, 775 (1981)].
10. A. I. Okorokov, V. V. Runov, B. P. Toperverg, et al., Pisma Zh. Eksp. Teor. Fiz. **43** (8), 390 (1986) [JETP Lett. **43**, 503 (1986)].
11. S. V. Grigoriev, S. V. Maleyev, V. V. Deriglazov, et al., Appl. Phys. A **74**, S719 (2002).
12. H. J. Kawamura, J. Phys. Soc. Jpn. **54**, 3220 (1985).
13. V. P. Plakhty, J. Kulda, D. Visser, et al., Phys. Rev. Lett. **85**, 3942 (2000).
14. S. V. Maleyev, V. G. Bar'yakhtar, and R. A. Suris, Fiz. Tverd. Tela **12**, 3461 (1971) [Phys. Solid State **12**, 2811 (1971)].
15. S. V. Grigoriev, S. V. Maleyev, A. I. Okorokov, et al., Phys. Rev. B **72**, 134420 (2005).
16. S. V. Maleyev, Phys. Rev. B **73**, 174402 (2006).
17. B. Lebech, J. Bernhard, and T. Freltoft, J. Phys. Condens. Matt. **1**, 6105 (1989).
18. S. V. Grigoriev, S. V. Maleyev, A. I. Okorokov, et al., Phys. Rev. B **73**, 224440 (2006).
19. C. Pfleiderer, G. J. McMullan, S. R. Julian, and G. C. Lonzarich, Phys. Rev. B **55**, 8330 (1997).
20. C. Pfleiderer, S. R. Julian, and G. G. Lonzarich, Nature **414**, 427 (2001).
21. C. Pfleiderer, D. Resnik, L. Pintschovius, et al., Nature **427**, 227 (2004).
22. S. V. Grigoriev, A. I. Okorokov, Yu. O. Chetverikov, et al., Pisma Zh. Eksp. Teor. Fiz. **83** (11), 568 (2006) [JETP Lett. **83**, 478 (2006)].
23. R. W. Erwin, J. J. Rhyne, M. B. Salamon, et al., Phys. Rev. **35**, 6808 (1987).
24. P. P. Du, A. M. Venter, et al., J. Phys. Condens. Matter **7**, 9863 (1995).
25. V. P. Plakhty, W. Schweika, Th. Bruckel, et al., Phys. Rev. B **64**, 100402 (2001).
26. S. V. Grigoriev, S. V. Maleyev, A. I. Okorokov, and H. Eckerlebe, Eur. Phys. Lett. **63**, 56–62 (2003).
27. P. J. Brown, J. Magn. Magn. Mater. **242-245**, 781 (2002).
28. Y. Ishikawa, S. Onodera, and K. Tajima, J. Magn. Magn. Mater. **10**, 183 (1979).
29. S. Onodera, Y. Ishikawa, and K. Tajima, J. Phys. Soc. Jpn. **50** (5), 1513 (1981).
30. M. M. Abd-Elmeguid and H. Micklitz, Physica B **161**, 17 (1989).
31. M. Matsushita, S. Endo, K. Miura, et al., J. Magn. Magn. Mater. **265**, 352 (2003).
32. P. Entel, E. Hoffmann, P. Mohn, et al., Phys. Rev. B **47** (14), 8706 (1993).
33. P. J. Webster, K. R. Ziebeck, and S. L. Town, Phylos. Mag. B **49**, 295 (1984).
34. A. N. Vasil'ev, V. D. Buchelnikov, T. Takagi, et al., Usp. Fiz. Nauk **173**, 577 (2003) [Phys.-Usp. **46**, 557 (2003)].
35. V. V. Runov, Yu. P. Chernenkov, M. K. Runova, et al., Zh. Eksp. Teor. Fiz. **102** (1), 102 (2006) [JETP **102**, 102 (2006)].
36. A. Vorobiev, J. Major, H. Dosch, et al., Phys. Rev. Lett. **93**, 267203 (2004).
37. S. V. Maleyev, Usp. Fiz. Nauk **172**, 617 (2002) [Phys.-Usp. **45**, 569 (2002)].
38. G. P. Kopitsa, S. V. Grigoriev, V. V. Runov, et al., Pisma Zh. Eksp. Teor. Fiz. **81**, 688 (2005) [JETP Lett. **81**, 556 (2005)].